

Laser-based K_α X-ray emission characterization using a high contrast ratio and high-power laser system

S. Fourmaux¹ · J. C. Kieffer¹

Received: 26 February 2016 / Accepted: 11 May 2016 / Published online: 26 May 2016
© Springer-Verlag Berlin Heidelberg 2016

Abstract We characterized a laser-based K_α X-ray source produced onto a Mo solid target. We used a laser system with a high laser pulse contrast ratio (LPCR) and an instantaneous power ~ 30 TW. We investigated simultaneously the K_α X-ray conversion efficiency, the X-ray source size, and the proton front surface emission. We found a high K_α X-ray conversion efficiency up to 2×10^{-4} associated with an X-ray source size only ~ 1.8 times larger than the laser focal spot for the highest intensities. We found that using a high LPCR laser pulse with 245 mJ per pulse is of interest to develop a laser-based X-ray imaging system as it can combine a high conversion efficiency with a small increase in the X-ray source size compared to the laser focal spot.

1 Introduction

High-power Ti:sapphire laser technology improvements since the 1980s give the opportunity to access commercial-type ultrafast laser system with high intensity, up to 10^{20} W cm⁻² range when focused, and high repetition rate, up to kHz. These high-power lasers permit the production of a variety of laser-based X-ray sources: K_α X-ray radiation using K_α characteristic lines [1], broadband backlighter using bremsstrahlung and free to bound recombination from a high-Z solid target [2], Betatron radiation [3], and Compton scattering [4]. Here, we will discuss K_α X-ray sources. When a laser pulse is focused onto a solid target

and reaches intensities in the range 10^{15} – 10^{19} W cm⁻², a plasma is produced and energetic electrons are accelerated into it. These hot electrons travel inside the cold target volume and generate X-ray radiation: K_α characteristic line emission and broad bremsstrahlung spectrum.

Laser-based K_α X-ray sources are of interest for imaging as the X-ray source size can be reduced down to 5–25 μ m range, thus allowing imaging with high spatial resolution and phase contrast imaging. The X-ray radiation energy can also be selected by changing the target material to adjust to the object thickness and density. Among potential applications, we can cite biomedical imaging [5], for example in vivo tomography of small animal cancer models [6], plant imaging (interaction of plant with soils) [7], climate study using dendrochronology, or sediments deposit imaging [8]. We mention briefly that similar applications could be achieved with other techniques, like X-ray tubes, but a small X-ray source size is obtained at the expense of the X-ray flux, or using a synchrotron facility, but accessibility of such big equipment is an issue. For practical applications, it is critical to get a high X-ray flux associated with a small X-ray source size. The high flux allows to realize micro-computed tomography (μ -CT) or to study a large number of samples in a reasonable amount of time. The small X-ray source size allows to keep a high resolution and a high imaging contrast. Thus, it is of importance, to reach this objective, to optimize the laser parameters available with the current laser technology.

Laser-based K_α X-ray sources have been studied by many laboratories since the 1970s using first nanosecond lasers, and more recently with picosecond and femtosecond lasers [1]. The value of the maximum achievable η_{K_α} , the laser energy to K_α X-rays photon conversion efficiency, has been reported to decrease with the target atomic number

✉ S. Fourmaux
fourmaux@emt.inrs.ca

¹ Institut National de la Recherche Scientifique - Énergie, Matériaux et Télécommunications (INRS-EMT), Université du Québec, 1650 Lionel Boulet, Varennes, QC J3X 1S2, Canada

Z [9]. Assuming a plasma density gradient $L/\lambda = 0.3$, the optimum intensity I_{opt} to get the highest η_{K_α} has been predicted to depend of the target material atomic number Z as follows $I_{\text{opt}}(\text{W cm}^{-2}) = 7 \times 10^9 \times Z^4$ [9]. For the plasma density gradient L/λ , L is the electronic gradient length and λ is the laser wavelength. $L = \frac{1}{N_e} \frac{dN_e}{dz}$, where N_e is the electronic density and z is the direction normal to the target surface. High conversion efficiencies have been demonstrated, up to $\eta_{K_\alpha} \sim 10^{-4}$, using laser systems with low laser pulse contrast ratio $\sim 10^6$ (LPCR, defined as the ratio between the laser pulse peak intensity and any pre-pulses or the pedestal intensity), but the size of these X-ray sources were from four to eight times the laser focal spot size [10–13]. It has been reported that to keep the X-ray source size close to the laser focal spot size, a high contrast laser pulse ratio must be used [10, 14–16]. This is related to a steep plasma density gradient L/λ [17].

An approach to achieve high X-ray brightness is to increase the repetition rate or use higher wavelength. In recent years, K_α X-ray sources have been extensively studied with femtosecond laser system operating up to the kHz repetition rate. Several works were reported using laser systems with repetition rates in the kHz range with Cu or Ga targets. However, the relatively low energy of the K_α lines from these materials make it ill-suited for imaging applications which require higher energy to penetrate cm of matter [12, 18–21]. Higher-energy K_α X-ray photons from heavy metals such as Ag or Mo have been used in a few experimental works [11, 15, 22]. For example, 600 mJ per laser pulse corresponding to an intensity $4 \times 10^{18} \text{ W cm}^{-2}$ has been used to produce K_α X-ray radiation with Ag targets at 10-Hz repetition rate. This resulted in 2×10^{-5} conversion efficiency and X-ray source sizes five times larger as compared to the 10- μm optical focal spot size. This is explained by the low LPCR utilized in the experiments which is, respectively, 10^4 for the picosecond pedestal, and 10^5 for nanosecond pre-pulses [11].

In this context, at INRS-EMT, we investigated the generation of K_α X-ray radiation using high-Z targets with second harmonics generation (400 nm) which permits to produce a high LPCR with an initially low contrast ratio laser system and to keep an X-ray source size close to the laser focal spot size (between one and three times larger) [17, 23]. To validate the approach consisting to increase the repetition rate, we used a 100-Hz repetition rate laser system exhibiting a thermal load before compression of 11 W [24, 25]. One drawback of using second harmonics generation is that it reduces the hot electrons' temperature T_h . This last one scales as $T_h \propto (I\lambda^2)^\alpha$, where I is the laser intensity and α is between $\frac{1}{3}$ and 1 depending of the numerical calculation assumptions for the laser absorption processes and the experimental results [26]. Thus, using second harmonics

generation reduces the conversion efficiency η_{K_α} which is optimum for $T_h \sim 2-6 \times E_{K_\alpha}$ [27, 28].

In this article, we report K_α X-ray production with a 100-TW-scale laser system with high energy (up to ~ 0.8 J per pulse), 10-Hz repetition rate, and high LPCR at the 800-nm fundamental wavelength (better than 10^{10} for times higher than 100 ps before the peak intensity). We determined the K_α X-ray conversion efficiency and correlated it with the X-ray source size and proton energy measured simultaneously for each laser shot. This work objective is to validate the interest to use such high LPCR laser technology and to determine what are the optimal parameters in terms of laser energy versus conversion efficiency and X-ray source size for X-ray imaging applications.

2 Experimental setup

2.1 Laser system

Experiments were performed using the 100-TW-class laser system at the Advanced Laser Light Source (ALLS) facility located at INRS-EMT. This Ti:sapphire-based laser system is a commercial prototype based upon the chirped pulse amplification technique (CPA). It has a central wavelength of 800 nm and a 55-nm bandwidth. During these experimental series, the maximum laser energy on target is $E_{\text{laser}} \sim 850$ mJ and the pulse duration is 30-fs full width at half maximum (FWHM). This results in ~ 30 TW of instantaneous power on target. Using a 27-cm focal length off-axis parabola, the beam is focused to 15 μm diameter (FWHM), with 30 % of laser energy delivered within this diameter. The maximum peak intensity on target is about $I_{\text{peak}} = 6 \times 10^{18} \text{ W cm}^{-2}$. For a convenience of the setup, and in order to maximize laser-plasma absorption, the laser angle of incidence on target is fixed at 45° and P-polarization is used (see Fig. 1).

This work follows some preliminary results obtained using a similar experimental setup, where to validate an LPCR enhancement technique, we measured separately the X-ray source size and the maximum proton energy in two LPCR conditions: nominal (low LPCR) and improved (high LPCR). We observed that the X-ray source size is reduced and the proton energy is increased when the LPCR is improved [29].

In nominal LPCR conditions, a saturable absorber (#1) is used before injection of the laser pulse into the regenerative amplifier. It is located in the booster, just before the stretcher as can be seen in Fig. 2. It supports a laser pulse contrast ratio close to 10^9 for a time 50 ps before the peak intensity. More precisely, we found a LPCR degradation for larger pulse delays before I_{peak} , especially between the interval 250 ps and 2.1 ns with a value close to 2.5×10^8 .

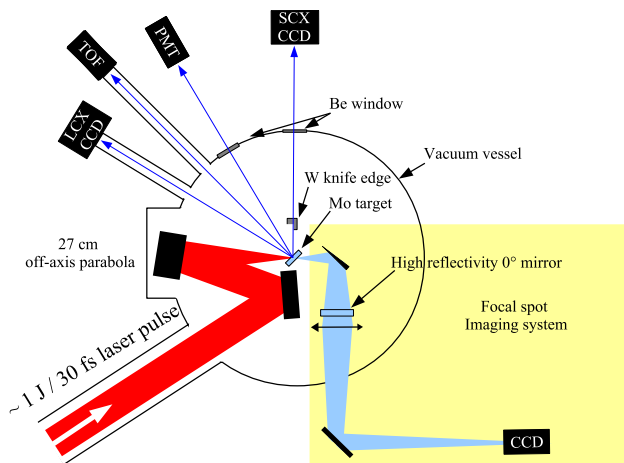


Fig. 1 Experimental setup (not at scale): The laser pulse is focused by an off-axis parabola and can be imaged by the focal spot imaging system. All the diagnostics are shown on the drawing: PMT, knife-edge imaging by an X-ray CCD (SCX), X-ray photon counting (LCX), and protons beams measurement (TOF)

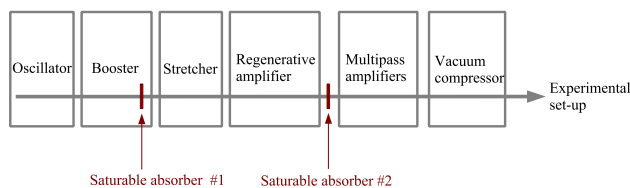


Fig. 2 Sketch of the laser system. The saturable absorbers positions in the laser system are indicated. The saturable absorber #1 is used with short laser pulses. The saturable absorber #2 is used with long chirped laser pulses

The highest pre-pulse originating from the regenerative amplifier exhibits a LPCR of 5.3×10^7 for a delay of 11 ns before the peak intensity.

In improved LPCR conditions, to improve the LPCR, an extra saturable absorber (#2) is inserted after the regenerative amplification stage. The LPCR is similar with and without the saturable absorber #2 up to 54 ps before I_{peak} . For longer delays, the LPCR is improved with the saturable absorber #2 and is found to be better than 10^{10} for times higher than 100 ps before the peak intensity. When the saturable absorber #2 is used, the pre-pulses intensity level originating from the regenerative amplifier decreases by two orders of magnitude.

A complete characterization of this laser system LPCR corresponding to these experimental series in the two LPCR conditions can be found in a previous publication [29]. This characterization is still valid for the present work where we focus our interest on the improved LPCR condition. Molybdenum damage threshold is $\sim 2 \text{ J/cm}^2$ for laser pulse duration below 380 ps and in normal incidence [30].

Obviously, with this high LPCR and in our energy regime, pre-pulses and the pedestal level are not a concern.

2.2 Diagnostics

Figure 1 shows the experimental configuration in the interaction vacuum vessel. The laser pulse is focused onto a thick molybdenum solid target by the use of an off-axis parabola, resulting in a peak intensity ranging from $I_{\text{peak}} = 5.7 \times 10^{16}$ up to $6.1 \times 10^{18} \text{ W cm}^{-2}$ on the target. A permanent imaging system allows to monitor the laser pulse spatial distribution at the target location with a 40 \times magnification. It consists of a wedge, a zero degree high-reflectivity mirror followed by a $f = 10 \text{ cm}$ lens, and a charge-coupled device (CCD) camera. Using this imaging system, we set the best focus with the smallest focal spot size at the target position. The target is moved continuously in order to get the beam interacting with a clean surface at each laser shot. The target holder permits to insure that at each laser shot, the target position along the laser propagation axis is stable within 10- μm precision which is much lower than the Rayleigh length. The target holder can be translated under vacuum to allow the beam to propagate at maximum energy into the imaging system or to set the target in position for laser interaction.

All diagnostics are positioned around the equatorial plane and are used simultaneously for every laser shot. The target is positioned at the vacuum vessel center toward which all the diagnostics are aligned. X-rays were monitored with a photomultiplier tube (PMT), filtered by a beryllium (Be) window (250 μm thick) and an Al plate (1 mm thick), at a distance of 90 cm to monitor the X-ray amplitude signal. The PMT measurement can be related to the K_{α} X-ray radiation and the bremsstrahlung radiation emitted for energies above $\sim 12 \text{ keV}$. This signal is used to confirm that the laser pulse is focused onto the target surface as the relative distance between the off-axis parabola and the target can be adjusted under vacuum by moving the off-axis parabola. Figure 3 shows the measured signal when the focus position is moved along the laser propagation axis (target position is at the abscissa axis origin). We observe that the highest signal corresponds to the laser pulse being focused close to the target (this is confirmed by the figure continuous line polynomial fit).

The X-ray spectra were measured by photon counting with a direct detection deep-depletion X-ray CCD (model PI-LCX thermoelectrically cooled), with 1024×256 imaging pixels of size $20 \mu\text{m} \times 20 \mu\text{m}$. The CCD quantum efficiency extends above 20 keV and is well fitted to measure the Mo characteristic line emission: $K_{\alpha 1}$ at 17.48 keV, $K_{\alpha 2}$ at 17.37 keV, and $K_{\beta 1}$ at 19.61 keV. This detector is connected to the vacuum vessel by a vacuum-tight tube, and a light-tight 6- μm Al filter is used in front of it. The

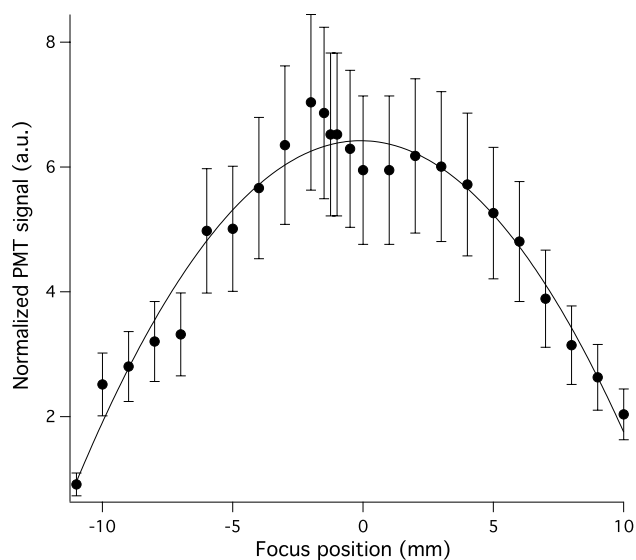


Fig. 3 Normalized PMT signal as a function of the relative distance between the off-axis parabola and the target. Target surface position is at the abscissa axis origin, and we defocus by moving the off-axis parabola (moving toward positive values means that the laser is focused before the target). This scan is achieved at 850 mJ energy. The error bars correspond to a typical 20 % standard deviation. The continuous line corresponds to a polynomial data fit

CCD camera is composed of a high number of independent detectors. Every single photon detected by one of these detectors gives a number of counts which is proportional to its energy. With our settings, the calibration factor is 0.091 count per eV by calibrating the X-ray CCD using K_{α} lines emitted in laser–solid interaction and known K -edge energies from metallic filters. If the number of photons per pixel is small compared to one, the measurement of the X-ray spectrum becomes possible by realizing a histogram. This histogram gives the number of occurrences of the same number of counts on one pixel as a function of the number of counts. A single photon produces electrons that might be collected by several neighboring pixels. It has to be taken into account to correctly reconstruct the spectra. We use an algorithm that only takes into account non-spreading events in which electrons are detected on only one pixel (single-pixel event). Thus, it is necessary to know the probability that a single photon yields a single-pixel event, $k1(\hbar\omega)$, which depends on the photon energy $\hbar\omega$. This function has been obtained from a simulation modeling the LCX CCD response and providing $k1(\hbar\omega)$ [31]. More details about the spectrum reconstruction method can be found in another publication [32]. In order to operate in photon counting mode, the X-ray CCD is positioned at a distance of 90 cm from the target as shown in Fig. 1, and the signal is attenuated using a Mo filter with a thickness of 100 μm .

The X-ray source size is measured using an indirect detection X-ray CCD (model PI-SCX4300

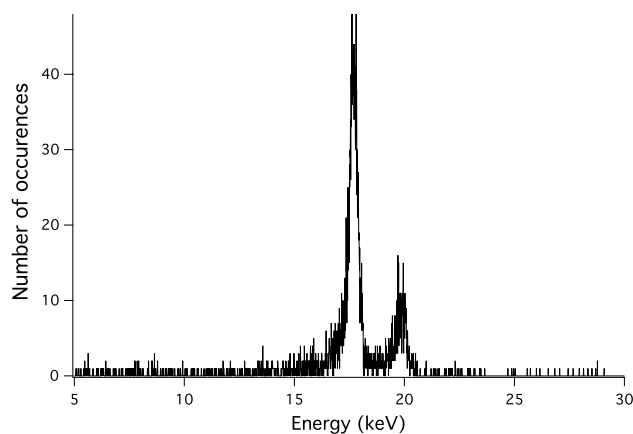


Fig. 4 Single-pixel event histogram obtained with one laser shot. It corresponds to an on-target intensity of $6 \times 10^{18} \text{ W cm}^{-2}$

thermoelectrically cooled) to image a knife-edge. The CCD is located 170 cm away from the target, and the knife-edge is positioned under vacuum 24 cm away from the target resulting in a 7 \times magnification. This CCD has 2084 \times 2084 imaging pixels of size 24 μm \times 24 μm . A Gd_2SO_2 scintillator screen optimized for 17 keV energy is coupled to the CCD by a fiber-optic faceplate permanently bonded to the chip (the CCD chip is under vacuum). The resulting spatial resolution is estimated to be below 6 μm in the object plane.

Protons beams are produced on the target surface by target normal sheath acceleration (TNSA) process and can be used to correlate the hot electron energy. To measure the energy of protons beams directed from the front target surface after laser irradiation, a time-of-flight (TOF) spectrometer is placed along the target normal axis. The TOF spectrometer consists of a vacuum tube leading to a plastic scintillator exposed to a PMT. The scintillator is protected by a light-tight Al filter, and the distance from target to scintillator is 1.65 m. More details about this spectrometer can be found in a previous publication [33].

3 Results and discussion

3.1 K_{α} X-ray conversion efficiency $\eta_{K_{\alpha}}$

Figure 4 presents a typical single-pixel event histogram (it corresponds to a raw spectrum where no full reconstruction has been achieved) obtained using the photon counting technique and a Mo target. The calculated Fano-limited resolution is ~ 207 eV for K_{α} lines energy which does not permit to resolve the Mo $K_{\alpha 1}$ and $K_{\alpha 2}$ lines emission [31]. The integrated K_{α} lines and the $K_{\beta 1}$ line are clearly resolved, and well above the bremsstrahlung continuous emission. The measured spectrum is mostly line emission, but some

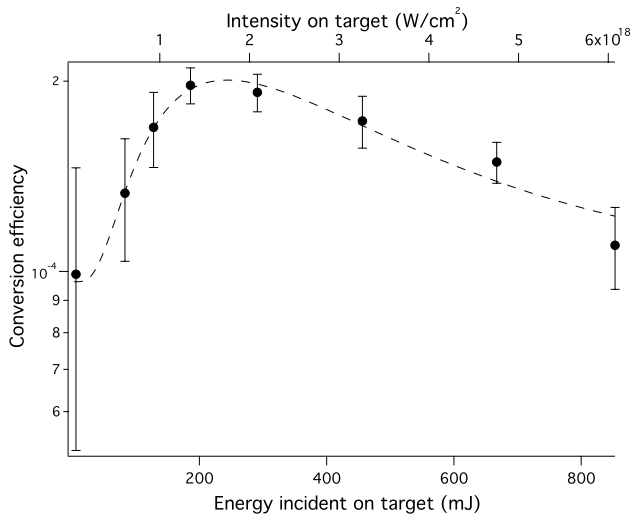


Fig. 5 Absolute conversion efficiency η_{K_α} from the laser light into the K_α line emission, as a function of the laser energy or the intensity incident on target. The dotted line is a lognormal function fit of the experimental points and is used as a guide for the eye

continuous bremsstrahlung can be observed before each K_α line. Using this spectrum measurement, we can determine the X-ray conversion efficiency.

The curve shown in Fig. 5 corresponds to the absolute conversion efficiency η_{K_α} (in 2π steradians), from the laser light into the K_α X-ray line emission, as a function of the on-target incident laser energy or intensity. The error bars correspond to the standard deviation on a statistics of at least five laser shots for every energy value. The dotted line corresponds to a lognormal fit of the experimental points and is used as a guide for the eye. The lognormal function is $a_1 + a_2 \times \exp\left(-\left(\frac{\ln(E/a_3)}{a_4}\right)^2\right)$, where a_1, a_2, a_3 , and a_4 are the fit parameters, and E is the energy incident on target.

The conversion efficiency is high and inside the interval 9.9×10^{-5} – 1.97×10^{-4} for all the considered energies. The best efficiency is found for a laser energy around 245 mJ which translates into an intensity of $1.75 \times 10^{18} \text{ W cm}^{-2}$. The correlation between high conversion efficiency and a high LPCR has already been reported in a previous publication when using the laser fundamental frequency [22]. For comparison with our previous results at INRS-EMT, using a frequency-doubled 200 mJ energy laser pulse corresponding to an intensity in the range of $10^{18} \text{ W cm}^{-2}$, a conversion efficiency $\eta_{K_\alpha} = 10^{-5}$ was measured at 10-Hz repetition rate [17, 23]. Using a frequency-doubled 20 mJ energy laser pulse, we found a conversion efficiency $\eta_{K_\alpha} = 1.5 \times 10^{-5}$ at 100-Hz repetition rate [25].

When the conversion efficiency reaches its highest value, it means that the hot electron energy is well matched for the Mo K_α line production. Thus, the hot electron temperature must be close to the optimum energy (~ 35 – 105 keV).

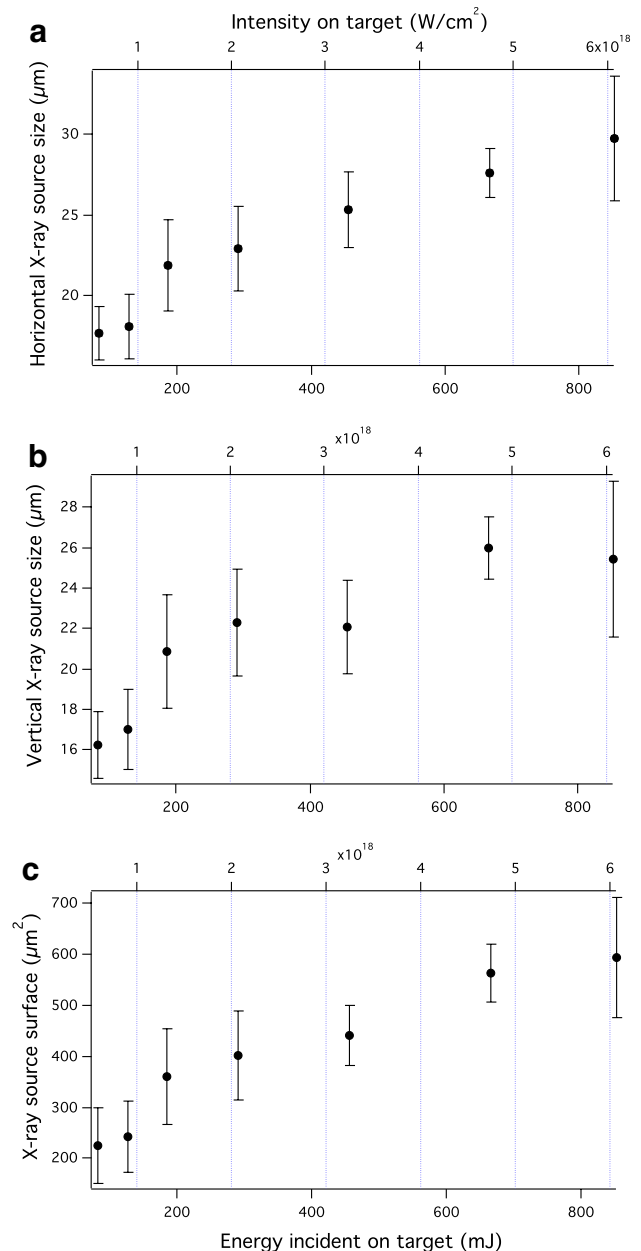


Fig. 6 X-ray source size characterization as a function of the on-target incident energy or intensity. **a** Measured FWHM diameter seen by the X-ray detector along the horizontal axis. **b** Measured FWHM diameter seen by the X-ray detector along the vertical axis. **c** Measured X-ray source surface

This optimum energy interval is rather large and does not allow a precise electron temperature determination. Above this energy, the hot electron temperature is much higher and energetic electrons penetrate deep inside the target. K_α photons are absorbed as they propagate in the target toward the surface which reduces the conversion efficiency η_{K_α} .

In this experiment LPCR condition, any pre-plasma production occurs in the rising edge of the laser pulse and we

expect a step-like plasma density profile. In this case, we assume that the laser energy is absorbed by the target electrons through a Brunel-like mechanism as is confirmed by a previous experiment where a high LPCR is obtained by using a double plasma mirror setup [34, 35]. In this case, $T_h = \alpha(I\lambda^2)^{1/3}$ and we can estimate α coefficient from previous works. Using PIC simulations, it was found that $\alpha = 7$ for Brunel-like mechanism [26]. From a previous experimental work, using 530-nm second harmonics generation to enhance the LPCR in the $10^{17} - 10^{18} \text{ W cm}^{-2}$ intensity regime on Ag targets, it can be determined that $\alpha \sim 8.6$ [15]. The coefficient can also be determined to be $\alpha \sim 6.3$ with another experimental study in the $10^{18} \text{ W cm}^{-2}$ intensity range and using 400-nm second harmonics generation [17]. Thus, we assume that $\alpha = 7$ which gives $T_h = 34 \text{ keV}$ at 245 mJ for the maximum conversion efficiency. This value is low, but still compatible with the expected energy interval.

3.2 X-ray source size

To measure the X-ray source spot size, a tungsten knife-edge (0.6 mm thick) is imaged simultaneously both along the horizontal and the vertical axes. The edge-spread function (ESF) obtained for each edge image is fitted with a Fermi function. The differentiation of this function yields the line-spread function, which is fitted by a Gaussian distribution [10].

The measured X-ray sources sizes (both along the vertical and the horizontal axes) as a function of the on-target incident energy or intensity are shown in Fig. 6a, b. The error bars correspond to the standard deviation on a statistics of at least five laser shots for every energy value. For the highest laser energy, the X-ray sources sizes are found to be up to ~ 1.8 times larger than the laser focal spot along both axes. When the laser energy is decreased, the X-ray source size is also decreasing down to a size similar to the laser focal spot. Note that, this behavior is similar to reference 29 results in the improved LPCR conditions (X-ray source surface were reported) as can be seen in Fig. 6c.

We already mentioned that X-ray sources size have been found to be from four to eight times larger than the laser focal spot size when low LPCR is used [10–13]. This can be explained by the presence of a large pre-plasma where electrons can travel on large distances in the lateral direction. On the contrary, when high LPCR has been used, the X-ray sources measured were only 2–3 times larger than the laser focal spot size [15, 17]. In this case, several contributions can explain the larger X-ray source size: First, when electrons leave the target surface and come back to it, due to electrostatic forces, they scatter into a larger area. On the other hand, the space charge field developing near the critical density produces a large electrostatic field

which slows down the electrons and gives an effective stopping distance a lot less than the expected one into a cold solid target [36]. Second, the X-ray sources size increase can be explained by the low-intensity wings of the incident laser pulse which is associated with a hot electron temperature scaling from the pulse maximum to its edge [10]. We believe that the moderate hot electron temperature expected from the scaling law found in the previous section is in agreement with the low increase in the X-ray source size compared to the laser focal spot size. We also understand that more work beyond the scope of this paper would be necessary to fully understand the hot electron transport in the plasma.

3.3 Protons beams measurements

We illustrate in this section, even if this is an indirect method, how proton beams can be used to get an idea of T_h . Protons beams are produced on the target laser irradiated front surface and are related to the hot electron generation. For the laser–matter interaction conditions used in this experiment, ions are primarily accelerated by the TNSA process. In this mechanism, relativistic electrons are produced by the laser pulse at the front surface. Penetrating freely through the target, these energetic electrons establish space charge sheath fields on the target surfaces, which then pull ions outward [37]. This mechanism is usually studied on the thin foil target's rear side (opposite to the laser irradiated front side surface) as in many laser systems the LPCR is too low to prevent a pre-plasma on the front side surface and efficiently produce a proton beam. It has already been demonstrated that with high LPCR conditions, the pre-pulses or pedestal is small and induces a low enough plasma expansion to be able to consider that both target surfaces remain planar at the arrival of the main pulse. Protons beams are then observed on both sides of the target [33, 34]. In this experiment, we use a thick target, so only the target's front surface can produce a proton beam.

In Fig. 7, we measure the maximum proton cutoff energy as a function of the on-target incident energy or intensity. The first observation is that the LPCR is high enough to observe protons beams over all the intensity range of this experiment. The proton cutoff energy increases linearly from 160 keV up to more than 800 keV. The proton cutoff energy is $\sim 400 \text{ keV}$ for the highest conversion efficiency $\eta_{K\alpha}$. Note that, the measured proton cutoff energy is similar to what is reported in reference 29 in this high LPCR condition.

We can estimate the proton cutoff energy using a simple isothermal fluid expansion model on the irradiated target surface where the acceleration time is fixed to take into account the energy transfer from the hot electron to the ions. Several publications describe in detail this

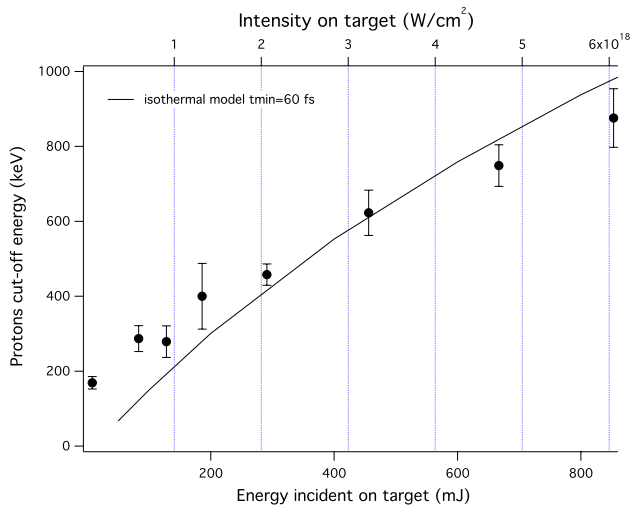


Fig. 7 Proton cutoff energy as a function of the on-target incident energy or intensity. Using a simple isothermal fluid expansion model, we calculated the expected proton cutoff energy for $t_{\min} = 60$ fs (continuous line)

analytical model [38, 39]. Figure 7 shows (in solid line) the resulting calculated maximum proton cutoff energy. We assume that T_h is given by a Brunel-like mechanism with $T_h = 7 \times (I\lambda^2)^{1/3}$. We use an effective acceleration time $t_{\text{acc}} = a \times (\tau + t_{\min})$, where τ is the laser pulse duration, the energy exchange time between electrons and protons is $t_{\min} = 60$ fs, and a varies linearly from 3 at the intensity $2 \times 10^{18} \text{ W cm}^{-2}$ to 1.3 at $3 \times 10^{19} \text{ W cm}^{-2}$ [40]. The laser light conversion fraction into hot electrons is given by $1.2 \times 10^{-15} I^{0.74}$ where I is the laser intensity [36, 41]. For such a simple model, the calculated maximum proton cut-off energies are in reasonable agreement with the measurements which comfort us with the estimated scaling law for the electron temperature.

3.4 Phase contrast imaging potential

We characterized the K_{α} X-ray source, and we can now assess its potential for in-line phase contrast imaging applications. To investigate it, we use a simple one-dimension numerical model to determine the imaging pattern from a reference object as a function of the X-ray source size. The reference object is a cylindrical nylon wire, whose refractive index is close to biological tissues and for which absorption is small in the hard X-ray range. In this model, we assume a monochromatic X-ray source with an energy of 17.4 keV. The wave amplitude at each point of a plane object is given by the Fresnel–Kirchoff integral calculated into the Fresnel approximation. The detailed model can be found in a previous publication [17].

The object is located 70 cm away from the X-ray source. The detector is positioned 1.4 m away from the

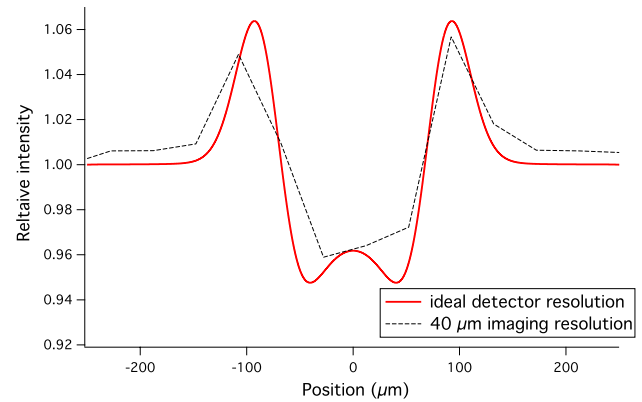


Fig. 8 Calculated X-ray diffraction pattern for a 15- μm X-ray source size and a 40- μm -diameter nylon fiber. The imaging magnification is 3. We show the result assuming ideal (continuous red line) and a 40- μm (dotted black line) imaging resolution in the detector plane

object giving a magnification of 3. This is similar to the experimental geometry used in previous experiments [17, 23]. The calculation is achieved with an X-ray source size ranging from 5 up to 40 μm which contains the measured X-ray source size interval from the current experimental series. We also vary the object diameter from 10 to 100 μm to know how many X-ray photons are required to observe the diffraction depending of the object characteristic dimension (in this case the diameter). To optimize the detection efficiency above 10 keV, a phosphor screen coupled to a CCD camera via a fiber-optic faceplate is usually used. As an example, we can consider the same Princeton Instrument CCD that has been used to measure the X-ray source size. This model is equipped with a phosphor screen optimized for 17 keV and with 68 % absorption efficiency at 17.4 keV. The typical spatial resolution in the detector plane is estimated to be around 40 μm . This gives an imaging resolution in the object plane of 13.3 μm in our geometry.

To illustrate this calculation, we show in Fig. 8, the calculated diffraction pattern for an X-ray source size of 15 μm , respectively, for the ideal detector (red line) and for a detector spatial resolution limited to 40 μm (dotted black line).

From the calculations, we can deduce the imaging contrast $C = \frac{H-L}{H+L}$, where H and L are the signals from the edge presenting, respectively, the highest and lowest intensities. It allows to calculate the total number of X-ray photons required to see the imaging pattern assuming it is limited by a Poisson noise. For example, in Fig. 8, the dotted line corresponds to $C = 0.04$. Assuming a Poisson noise, we need at least 625 absorbed X-ray photons on each CCD pixel to see the diffracted pattern. This corresponds to a total number of photon $N_{\text{Pois.}} = 4.4 \times 10^{13}$ photons emitted in 2π steradians.

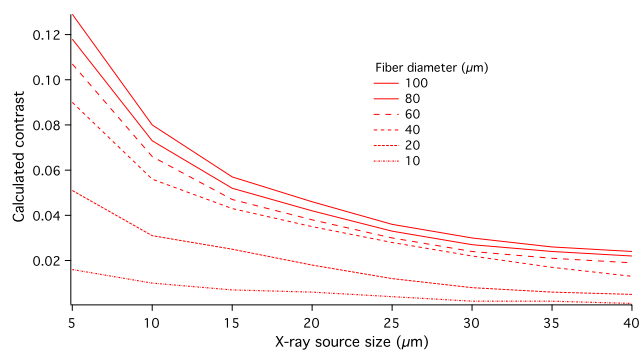


Fig. 9 Calculated imaging contrast as a function of the X-ray source size and for different objects diameter. The imaging resolution in the detector plane is $40\ \mu\text{m}$

In Fig. 9, we show the calculated imaging contrast C as a function of the X-ray source size and for different objects diameter. The spatial resolution at the detector plane is $40\ \mu\text{m}$. We observe that C the imaging contrast decreases when the X-ray source size is increased, and C is higher for increasing objects diameter. We note that C is low for object diameters lower than $40\ \mu\text{m}$. Assuming that there is no other noise source to mask the signal apart from the Poisson noise, it means a high number of photons are needed to be able to see the diffraction pattern.

In previous works, the typical number of laser shots to realize a phase contrast image is 4500. In this case, the source to detector distance is $215\ \text{cm}$, $\eta_{K\alpha} = 10^{-5}$ (with Ag $K\alpha$), and the energy per laser shot is $200\ \text{mJ}$ [17, 23]. At 10-Hz repetition rate, the experimental acquisition time required for each image is typically $t_{\text{exp}} = 7.5\ \text{min}$, which limits applications requiring a large number of images. The measured imaging contrast is $C = 0.047$. This requires $N_{\text{Pois.}} = 3.4 \times 10^{13}$ photons emitted in 2π steradians to measure the diffraction pattern. In practice, the number of photons corresponding to 4500 laser shot is around 15 times lower as line-out are realized by integrating the profile over several pixels (typically more than 15 pixels) to observe the profile of an object edge.

Using a laser source similar to our current work with high LPCR, we can assume an optimal conversion efficiency $\eta_{K\alpha} = 2 \times 10^{-4}$ and $245\ \text{mJ}$ per laser shot. This means that the X-ray source size is between 20 and $25\ \mu\text{m}$. For a $40\ \mu\text{m}$ object diameter, we find $C = 0.028$. To observe the corresponding diffraction pattern, it requires $N_{\text{Pois.}} = 9 \times 10^{13}$ photons emitted in 2π steradians. This number of photons corresponds to 5000 laser shots and $51\ \text{s}$ of laser shots at 100-Hz repetition rate. In practice, to see the diffraction pattern on a line-out, the total number of photons can be lower by a factor of 15 and correspond to $t_{\text{exp}} = 3.5\ \text{s}$. Thus, applications such as X-ray tomography

that require large acquisitions number would be within reach using the current commercial Ti:sapphire technology.

We already mentioned that another strategy to increase the X-ray flux for imaging applications is using higher repetition rate laser system. To evaluate it, we can assume a kHz laser system at $800\ \text{nm}$ wavelength with a high LPCR delivering $40\ \text{mJ}$ of energy per laser pulse. In this case, the X-ray source diameter is similar to the laser spot size and $C = 0.04$. Using the same calculation, we determine that $t_{\text{exp}} = 2.1\ \text{s}$ in order to observe the diffraction pattern of a $40\ \mu\text{m}$ object diameter with a line-out. We see that the accumulation time is similar to the previous case, but now the thermal load is $40\ \text{W}$ instead of $24.5\ \text{W}$ which might have an impact on the X-ray source efficiency and stability [24]. We understand that studying the thermal load influence onto the $K\alpha$ X-ray source is beyond the scope of this article.

4 Conclusion

We characterized a laser-based $K\alpha$ X-ray source produced by focusing a laser pulse onto a Mo solid target. We used a high LPCR and an instantaneous power $\sim 30\ \text{TW}$. We found a high $K\alpha$ X-ray conversion efficiency close to 2×10^{-4} associated with an X-ray source size close to the laser focus diameter: up to ~ 1.8 times larger for the highest intensity in this study ($\sim 6 \times 10^{18}\ \text{W cm}^{-2}$). We measured the proton production at the front side of the target and found $\sim 400\ \text{keV}$ for the best $\eta_{K\alpha}$. Our results are in agreement with a Brunel-like mechanism for the hot electron generation and a scaling law for the electron temperature $T_h = 7 \times (I\lambda^2)^{1/3}$. We assessed the quality of in-line phase contrast imaging with such a $K\alpha$ X-ray source and found that using a high LPCR laser system providing an energy per laser pulse of $245\ \text{mJ}$ and a repetition rate of $100\ \text{Hz}$ could be a good candidate to develop a laser-based X-ray imaging system with small acquisition time.

Acknowledgments We thank ALLS technical team for their support, especially Stéphane Payeur for his constant support. The ALLS facility was funded by the Canadian Foundation for Innovation (CFI). We acknowledge financial support from NSERC and the Canada Research Chair program.

References

1. J.C. Kieffer, A. Krol, Z. Jiang, C.C. Chamberlain, E. Scalzetti, Z. Ichalalene, Future of laser-based X-ray sources for medical imaging. *Appl. Phys. B* **74**(1), s75–s81 (2002)
2. F. Ráksi, K.R. Wilson, Z. Jiang, A. Ikhlef, C.Y. Côté, J.-C. Kieffer, Ultrafast X-ray absorption probing of a chemical reaction. *J. Chem. Phys.* **104**(15), 6066–6069 (1996)

3. A. Rousse, K. TaPhuoc, R. Shah, A. Pukhov, E. Lefebvre, V. Malka, S. Kiselev, F. Burgy, J.-P. Rousseau, D. Umstadter, D. Hulin, Production of a keV X-ray beam from synchrotron radiation in relativistic laser-plasma interaction. *Phys. Rev. Lett.* **93**, 135005 (2004)
4. K. Ta Phuoc, S. Corde, C. Thauray, V. Malka, A. Tafzi, J.P. Goddet, R.C. Shah, S. Sebban, A. Rousse, All-optical Compton gamma-ray source. *Nat Photon* **6**(5), 308–311 (2012)
5. R.A. Lewis, Medical phase contrast X-ray imaging: current status and future prospects. *Phys. Med. Biol.* **49**(16), 3573 (2004)
6. A. Krol, H. Ye, R. Kincaid, J. Boone, M. Servol, J.-C. Kieffer, Y. Nesterets, T. Gureyev, A. Stevenson, S. Wilkins, E. Lipson, R. Toth, A. Pogany, I. Coman, Mean absorbed dose to mouse in micro-CT imaging with an ultrafast laser-based X-ray source. *Proc. SPIE* **6510**, 65103P-1–65103P-6 (2007)
7. E. Lombi, J. Susini, Synchrotron-based techniques for plant and soil science: opportunities, challenges and future perspectives. *Plant Soil* **320**(1–2), 1–35 (2009)
8. S.C. Dufour, G. Desrosiers, B. Long, P. Lajeunesse, M. Gagnoud, J. Labrie, P. Archambault, G. Stora, A new method for three-dimensional visualization and quantification of biogenic structures in aquatic sediments using axial tomodesitometry. *Limnol. Oceanogr. Methods* **3**(8), 372–380 (2005)
9. C. Reich, P. Gibbon, I. Uschmann, E. Förster, Yield optimization and time structure of femtosecond laser plasma k_{α} sources. *Phys. Rev. Lett.* **84**, 4846–4849 (2000)
10. D.C. Eder, G. Pretzler, E. Fill, K. Eidmann, A. Saemann, Spatial characteristics of k radiation from weakly relativistic laser plasmas. *Appl. Phys. B* **70**(2), 211–217 (2000)
11. L.M. Chen, P. Forget, S. Fourmaux, J.C. Kieffer, A. Krol, C.C. Chamberlain, B.X. Hou, J. Nees, G. Mourou, Study of hard X-ray emission from intense femtosecond Ti:sapphire laser–solid target interactions. *Phys. Plasmas* **11**(9), 4439–4445 (2004)
12. C.G. Serbanescu, J.A. Chakera, R. Fedosejevs, Efficient k-alpha X-ray source from submillijoule femtosecond laser pulses operated at kilohertz repetition rate. *Rev. Sci. Instrum.* **78**(10), 569–575 (2007)
13. D. Boschetto, G. Mourou, A. Rousse, A. Mordovanakis, B. Hou, J. Nees, D. Kumah, R. Clarke, Spatial coherence properties of a compact and ultrafast laser-produced plasma keV X-ray source. *Appl. Phys. Lett.* **90**(1), 011106 (2007)
14. A. Rousse, P. Audebert, J.P. Geindre, F. Fallières, J.C. Gauthier, A. Mysyrowicz, G. Grillon, A. Antonetti, Efficient k_{α} X-ray source from femtosecond laser-produced plasmas. *Phys. Rev. E* **50**, 2200–2207 (1994)
15. J. Yu, Z. Jiang, J.C. Kieffer, A. Krol, Hard X-ray emission in high intensity femtosecond laser–target interaction. *Phys. Plasmas* **6**(4), 1318–1322 (1999)
16. N. Zhavoronkov, Y. Gritsai, G. Korn, T. Elsaesser, Ultra-short efficient laser-driven hard X-ray source operated at a kHz repetition rate. *Appl. Phys. B* **79**(6), 663–667 (2004)
17. R. Toth, S. Fourmaux, T. Ozaki, M. Servol, J.C. Kieffer, R.E. Kincaid, A. Krol, Evaluation of ultrafast laser-based hard X-ray sources for phase-contrast imaging. *Phys. Plasmas* **14**(5), 053506 (2007)
18. Y. Jiang, T. Lee, W. Li, G. Ketwaroo, C.G. Rose-Petruck, High-average-power 2-kHz laser for generation of ultrashort X-ray pulses. *Opt. Lett.* **27**(11), 963–965 (2002)
19. G. Korn, A. Thoss, H. Stiel, U. Vogt, M. Richardson, T. Elsaesser, M. Faubel, Ultrashort 1-kHz laser plasma hard X-ray source. *Opt. Lett.* **27**(10), 866–868 (2002)
20. A. Bonvalet, A. Darmon, J.-C. Lambry, J.-L. Martin, P. Audebert, 1 kHz tabletop ultrashort hard X-ray source for time-resolved X-ray protein crystallography. *Opt. Lett.* **31**(18), 2753–2755 (2006)
21. J. Weisshaupt, V. Juvé, M. Holtz, S.A. Ku, M. Woerner, T. Elsaesser, S. Ališauskas, A. Pugžlys, A. Baltuška, High-brightness table-top hard X-ray source driven by sub-100-femtosecond mid-infrared pulses. *Nat. Photon.* **8**(12), 927–930 (2014)
22. Z. Zhang, M. Nishikino, H. Nishimura, T. Kawachi, A.S. Pirozhkov, A. Sagisaka, S. Orimo, K. Ogura, A. Yogo, Y. Okano, S. Ohshima, S. Fujioka, H. Kiriyama, K. Kondo, T. Shimomura, S. Kanazawa, Efficient multi-keV X-ray generation from a high-z target irradiated with a clean ultra-short laser pulse. *Opt. Express* **19**(5), 4560–4565 (2011)
23. R. Toth, J.C. Kieffer, S. Fourmaux, T. Ozaki, A. Krol, In-line phase-contrast imaging with a laser-based hard X-ray source. *Rev. Sci. Instrum.* **76**(8), 083701 (2005)
24. S. Fourmaux, C. Serbanescu, L. Lecherbourg, S. Payeur, F. Martin, J.C. Kieffer, Investigation of the thermally induced laser beam distortion associated with vacuum compressor gratings in high energy and high average power femtosecond laser systems. *Opt. Express* **17**(1), 178–184 (2009)
25. S. Fourmaux, C. Serbanescu, R.E. Kincaid, A. Krol, J.C. Kieffer, K X-ray emission characterization of 100 Hz, 15 mJ femtosecond laser system with high contrast ratio. *Appl. Phys. B* **94**(4), 569–575 (2009)
26. P. Gibbon, *Short Pulse Laser Interactions with Matter: An Introduction* (Imperial College Press, London, 2005)
27. D. Salzmann, C. Reich, I. Uschmann, E. Förster, P. Gibbon, Theory of k_{α} generation by femtosecond laser-produced hot electrons in thin foils. *Phys. Rev. E* **65**, 036402 (2002)
28. J.C. Kieffer, A. Krol, System and method for generating micro-focused laser-based X-rays for mammography, December 27 2005. US Patent 6,980,625
29. S. Fourmaux, S. Payeur, S. Buffechoux, P. Lassonde, C. St-Pierre, F. Martin, J.-C. Kieffer, Pedestal cleaning for high laser pulse contrast ratio with a 100 TW class laser system. *Opt. Express* **19**(9), 8486–8497 (2011)
30. P.B. Corkum, F. Brunel, N.K. Sherman, T. Srinivasan-Rao, Thermal response of metals to ultrashort-pulse laser excitation. *Phys. Rev. Lett.* **61**, 2886–2889 (1988)
31. C. Fourment, N. Arzam, C. Bonte, T. Caillaud, D. Descamps, F. Dorchies, M. Harmand, S. Hulin, S. Petit, J.J. Santos, Broadband, high dynamics and high resolution charge coupled device-based spectrometer in dynamic mode for multi-keV repetitive X-ray sources. *Rev. Sci. Instrum.* **80**(8), 083505 (2009)
32. S. Fourmaux, S. Corde, P.K. Ta, P.M. Leguay, S. Payeur, P. Lassonde, S. Gnedyuk, G. Lebrun, C. Fourment, V. Malka, S. Sebban, A. Rousse, J.C. Kieffer, Demonstration of the synchrotron-type spectrum of laser-produced betatron radiation. *New J. Phys.* **13**(3), 033017 (2011)
33. S. Fourmaux, S. Buffechoux, B. Albertazzi, D. Capelli, A. Lévy, S. Gnedyuk, L. Lecherbourg, P. Lassonde, S. Payeur, P. Antici, H. Pépin, R.S. Marjoribanks, J. Fuchs, J.C. Kieffer, Investigation of laser-driven proton acceleration using ultra-short, ultra-intense laser pulses. *Phys. Plasmas* **20**(1), 013110 (2013)
34. T. Ceccotti, A. Lévy, H. Popescu, F. Réau, P. d'Oliveira, P. Monot, J.P. Geindre, E. Lefebvre, P. Martin, Proton acceleration with high-intensity ultrahigh-contrast laser pulses. *Phys. Rev. Lett.* **99**(18), 1–4 (2007)
35. A. Levy, T. Ceccotti, H. Popescu, F. Reau, P. D'Oliveira, P. Monot, P. Martin, J. Geindre, E. Lefebvre, Proton acceleration with high-intensity laser pulses in ultrahigh contrast regime. *IEEE Trans. Plasma Sci.* **36**(4), 1808–1811 (2008)
36. T. Feurer, W. Theobald, R. Sauerbrey, I. Uschmann, D. Altenbernd, U. Teubner, P. Gibbon, E. Förster, G. Malka, J.L. Miquel, Onset of diffuse reflectivity and fast electron flux inhibition in 528-nm-laser solid interactions at ultrahigh intensity. *Phys. Rev. E* **56**, 4608–4614 (1997)
37. S.C. Wilks, A.B. Langdon, T.E. Cowan, M. Roth, M. Singh, S. Hatchett, M.H. Key, D. Pennington, A. MacKinnon, R.A.

- Snively, Energetic proton generation in ultra-intense laser–solid interactions. *Phys. Plasmas* **8**(2), 542 (2001)
38. P. Mora, Plasma expansion into a vacuum. *Phys. Rev. Lett.* **90**(18), 16–19 (2003)
39. J. Fuchs, P. Antici, E. d’Humières, E. Lefebvre, M. Borghesi, E. Brambrink, C.A. Cecchetti, M. Kaluza, V. Malka, M. Manclossi, S. Meyroneinc, P. Mora, J. Schreiber, T. Toncian, H. Pépin, P. Audebert, Laser-driven proton scaling laws and new paths towards energy increase. *Nat. Phys.* **2**(1), 48–54 (2005)
40. J. Fuchs, Y. Sentoku, E. d’Humières, T.E. Cowan, J. Cobble, P. Audebert, A. Kemp, A. Nikroo, P. Antici, E. Brambrink, A. Blazevic, E.M. Campbell, J.C. Fernández, J.-C. Gauthier, M. Geissel, M. Hegelich, S. Karsch, H. Popescu, N. Renard-LeGalloudec, M. Roth, J. Schreiber, R. Stephens, H. Pépin, Comparative spectra and efficiencies of ions laser-accelerated forward from the front and rear surfaces of thin solid foils. *Phys. Plasmas* **14**(5), 053105 (2007)
41. M.H. Key, M.D. Cable, T.E. Cowan, K.G. Estabrook, B.A. Hammel, S.P. Hatchett, E.A. Henry, D.E. Hinkel, J.D. Kilkenny, J.A. Koch, W.L. Kruer, A.B. Langdon, B.F. Lasinski, R.W. Lee, B.J. MacGowan, A. MacKinnon, J.D. Moody, M.J. Moran, A.A. Offenberger, D.M. Pennington, M.D. Perry, T.J. Phillips, T.C. Sangster, M.S. Singh, M.A. Stoyer, M. Tabak, G.L. Tietbohl, M. Tsukamoto, K. Wharton, S.C. Wilks, Hot electron production and heating by hot electrons in fast ignitor research. *Phys. Plasmas* **5**(5), 1966–1972 (1998)